NiFe Nanoalloys Derived from Layered Double Hydroxides for Photothermal Synergistic Reforming of CH_4 with CO_2

Jiaqing Zhao, Xiangdong Guo, Run Shi, Geoffrey I. N. Waterhouse, Xuerui Zhang, Qing Dai, and Tierui Zhang**

Dry reforming of methane (DRM) with carbon dioxide to produce syngas is currently attracting a lot of attention for converting greenhouse gases into valuable chemicals. However, harsh reaction conditions in thermal catalysis hinder practical applications. Herein, a series of alumina-supported Ni_xFe_y nanoalloys are synthesized from NiFeAl-layered double hydroxide precursors, with the obtained catalysts used for photothermal synergistic DRM. The Ni_3Fe_1 nanoalloy catalyst shows a syngas production rate of 0.96 mol g^{-1} h^{-1} under a 350 °C photothermal condition, which is about 1100 times higher than that of the same catalyst at the same temperature in the dark. Methane activation as the rate-determining step in DRM is greatly enhanced by the localized surface plasmon resonance of the Ni_3Fe_1 nanoalloy in the ultraviolet region, thus accounting for the remarkably reduced reaction temperature. Meanwhile, the nanoalloy-based photothermal synergistic DRM exhibits sunlight-driven feasibility and 20 h of continuous operational stability.

1. Introduction

Modern societies are heavily reliant on fossil fuel energy, leading to high atmospheric greenhouse gas concentrations.[1] The discovery of technologies for reducing greenhouse gas emissions (especially CO_2 and CH_4) is presently the focus of intense worldwide research. While CO_2 is the primary anthropogenic greenhouse gas, CH_4 is often overlooked due to its lower abundance. However, huge amounts of methane are concentrated in arctic permafrost, which, if released through global warming, would have a devastating effect since the greenhouse gas heating effect of CH_4 is 20 times higher than CO_2 owing to its superior light-absorbing ability.[2] This motivates research to artificially capture and transform CO_2 and CH_4 into useful chemicals.[3]

Catalytic conversion technologies driven by clean energy offer tremendous promise for converting CO_2 and CH_4 into valuable chemicals with minimal secondary harm to the environment.[3b,4] Dry reforming of methane (DRM, $CH_4 + CO_2 \rightarrow 2CO + 2H_2$) simultaneously converts two greenhouse gases into syngas ($CO+H_2$), with the latter being an essential feedstock in the chemical industry for the preparation of long-chain alkanes, alkenes, and other commodity chemicals.[5] Transition metal catalysts (Ni, Co, Fe, etc.) and some precious metal catalysts (Ru, Pt) supported by appropriate carriers (SiO_2, TiO_2, zeolite, etc.) are active for the DRM reaction.[6] However, since CH_4 and CO_2 have high bond energies of 413 kJ mol^{-1} (C—H) and 803 kJ mol^{-1} (C=O), respectively, elevated temperatures (>1000 °C) and pressurization (>2 MPa) are often needed to drive the reaction.[6a,d] Such harsh reaction conditions increase the cost of the reaction process and lead to severe catalyst deactivation.[5a,7]

In recent years, photo-driven catalysis has been widely pursued as an alternative to traditional thermal catalytic reactions, including nitrogen fixation, CO_2 reduction, and Fischer–Tropsch synthesis.[8] Unlike low-temperature photocatalysis, photothermal catalysis typically shows very high conversion efficiencies.[8d,9] The photothermal effect raises the surface

---

J. Zhao, R. Shi, X. Zhang, T. Zhang
Key Laboratory of Photochemical Conversion and Optoelectronic Materials
Technical Institute of Physics and Chemistry
Chinese Academy of Sciences
Beijing 100190, China
E-mail: shirun@mail.ipc.ac.cn; tierui@mail.ipc.ac.cn

J. Zhao, X. Guo, X. Zhang, Q. Dai, T. Zhang
Center of Materials Science and Optoelectronics Engineering
University of Chinese Academy of Sciences
Beijing 100049, China

X. Guo, Q. Dai
CAS Key Laboratory of Nanophotonic Materials and Devices
CAS Key Laboratory of Standardization and Measurement for Nanotechnology
CAS Center for Excellence in Nanoscience
National Center for Nanoscience and Technology
Beijing 100190, China

R. Shi
Key Laboratory of Thermal Management and Energy Utilization of Aircraft
Ministry of Industry and Information Technology
Nanjing 210016, China

G. I. N. Waterhouse
School of Chemical Sciences
The University of Auckland
Auckland 1142, New Zealand

temperature of the catalyst through a strong light absorption in visible and near infrared regions, typically achieving a reaction efficiency similar to or even higher than the thermal catalysis in the dark.[9] Pioneering research by Ye and Hu et al. demonstrated that the DRM could be enhanced by introducing visible light (or part of its spectrum) to stimulate the localized surface plasmon resonance (LSPR) of noble-metal-based catalysts.[8a,b] However, its limitation lies in the poor utilization of ultraviolet (UV) photons, which show weak photothermal effects but could excite catalysts to generate energetic charge carriers to promote the reaction kinetics.[10] Achieving a photo-driven DRM reaction with a high solar spectral utilization efficiency, mild reaction conditions, and long-term operation stability using earth-abundant non-precious metal-based catalysts has proved elusive to date.

Herein, a series of novel NiFe nanoalloy catalysts supported by amorphous Al_2O_3 with different Ni:Fe molar ratios were fabricated by H_2 reduction of NiFeAl layered double hydroxide (LDH) nanosheets (the obtained catalysts are denoted as Ni_xFe_y, where x and y are molar amounts of Ni and Fe). The alumina-supported Ni_3Fe_1 nanoalloy catalyst delivered a photo-driven DRM syngas production rate up to 0.96 mol g^{-1} h^{-1} under xenon lamp irradiation. Similar catalytic performance can be obtained using concentrated sunlight as the light source. Through electromagnetic field simulations and in situ infrared spectroscopy, the outstanding activity of the Ni_3Fe_1 nanoalloy catalyst resulted from a synergistic effect involving photothermal heating and LSPR enhancement in the visible and UV regions, respectively. The synergistic effect lowers the apparent activation energy of methane and promotes its reforming with CO_2, thus allowing syngas production at low temperatures (as low as at 100 °C) and with excellent operating stability in 20 h tests.

2. Results and Discussions

The Ni_xFe_y catalysts used in photothermal catalytic DRM reaction tests were prepared by direct H_2 reduction of NiFeAl-LDH nanosheets in an H_2/Ar (10/90, v/v) atmosphere at 650 °C. The morphology of LDH nanosheet precursors was first characterized by transmission electron microscopy (TEM) and high-resolution TEM. LDH precursors with different NiFe proportions were prepared. Each precursor was comparable in size, possessing a thickness of 5 nm and a lateral size of 200–400 nm (Figures S1 and S2, Supporting Information). Element contents in the precursors and derived Ni_xFe_y catalysts were verified by energy-dispersive X-ray (EDX) element analysis (Figures S3 and S4, Supporting Information). **Figure 1**a,b shows TEM images of the

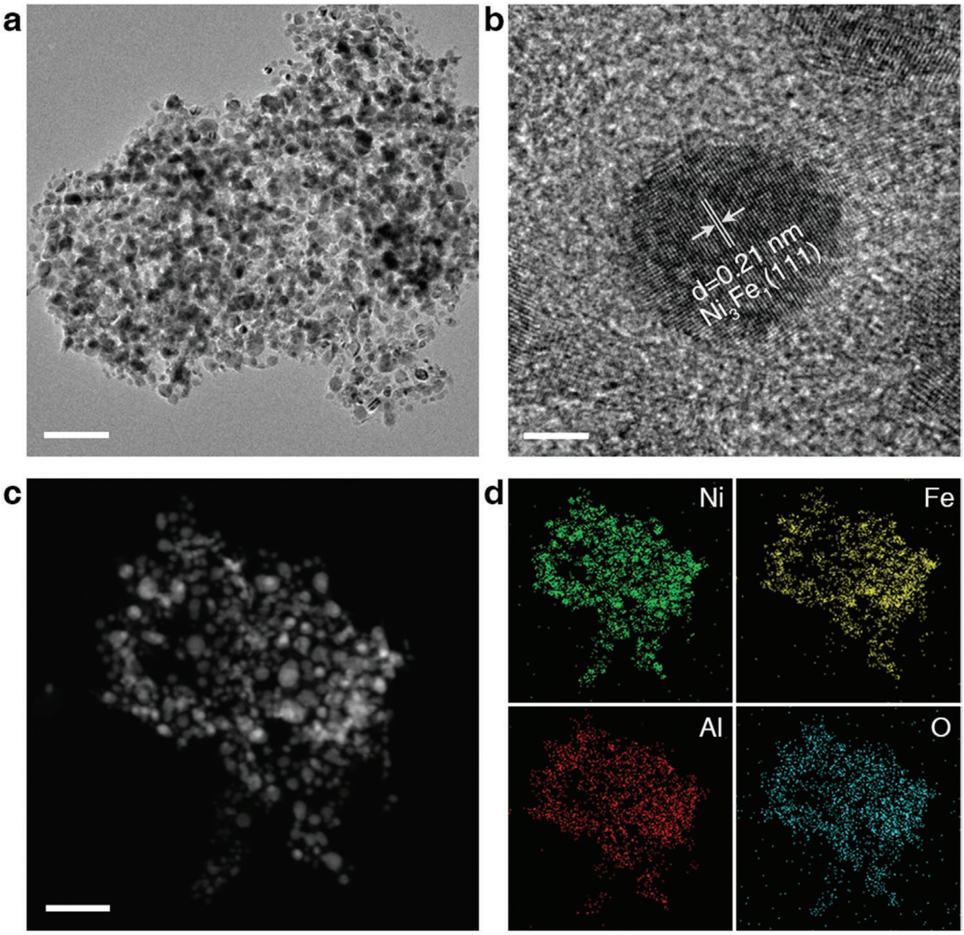

Figure 1. Morphological characterization of the Ni_3Fe_1 catalyst. a) TEM image. Scale bar: 100 nm. b) HRTEM image. Scale bar: 5 nm. c) HAADF-STEM image. Scale bar: 100 nm. d) Overlayed EDX element map and individual EDX maps for Ni, Fe, Al, and O.

Ni_3Fe_1 catalyst (taken as a representative example). The sample consists of nanosheet-supported metal particles. The lateral size of the nanosheets was similar to that of the LDH precursor, with the metal nanoparticles having an average particle size of about 20 ± 10 nm. The lattice fringe spacing on the nanoparticles was measured to be 0.21 nm, corresponding to the (111) crystal plane spacing of Ni_3Fe_1 alloy. High angle annular dark field-scanning transmission electron microscopy (HAADF-STEM) and EDX elemental mapping were used to characterize the elemental distribution of the catalysts after hydrogen reduction. The results (Figure 1c,d) show that Ni and Fe elements in the catalyst after hydrogen reduction were homogeneously distributed in the nanoparticles, while O and Al elements were uniformly dispersed in nanosheets, consistent with the formation of alumina supported Ni_3Fe_1 nanoalloys. EDX line over several adjacent nanoparticles (Figure S5, Supporting Information) provided further evidence for a homogeneous distribution of Co and Fe in the nanoparticles.

The structure and chemical state of the Ni_xFe_y catalysts and their LDH precursors were further characterized by X-ray diffraction (XRD) and X-ray photoelectron spectroscopy (XPS). The XRD (Figure S6, Supporting Information) patterns for the LDH precursors show characteristic (003), (006), and (009) peaks, consistent with LDH materials.[4] The absence of these peaks after the high-temperature hydrogen reduction step indicated the collapse of the LDH structure. Hydrogen reduction of the Ni_3Fe_1Al-LDH sample gave rise to XRD peaks typical for Ni_3Fe_1 alloy (peaks at 44.27°, 51.53°, and 75.86° being readily assigned to (111), (200), and (220) reflections, respectively; JCPDS-38-0419). For the samples with Ni:Fe mole ratios less than 3:1 or greater than 3:1, peaks of metallic Fe (44.27°, 51.53°, and 75.86°, due to (111), (200), and (220) reflections, respectively: JCPDS-65-4150) or Ni (44.34°, 51.67°, and 76.09°, due to (111), (200), and (220) reflections, respectively; JCPDS-65-0380) appeared, indicating the formation of discrete Fe and Ni metal nanoparticles rather than nanoalloys. For all Ni_xFe_y catalysts, no peak of Al_2O_3 was observed, indicating that the alumina was present as amorphous alumina.[4,9,10] For an oxide control sample by calcinating Ni_3Fe_1Al-LDH in the air at 650 °C, peaks of trevorite $NiFe_2O_4$ were found (37.32°, 43.38°, and 63.02°, corresponding to (222), (400) and (440) reflections, respectively; JCPDS-56-0964). XPS spectra reveal that Ni and Fe in the LDH precursors and oxide samples existed in the +2 and +3 valence states, respectively.[10] For Ni_xFe_y, both Fe and Ni were predominantly present in metallic form (Figure S6b,c, Supporting Information).

Ni K-edge and Fe K-edge X-ray absorption near-edge structure (XANES) and extended X-ray absorption fine structure (EXAFS) were used to characterize the local coordination of Fe and Ni in the catalysts and precursors. Figure S7, Supporting Information, shows that LDH precursors and the $NiFe_2O_4$ control sample contained Ni and Fe in valence states similar to NiO and Fe_2O_3. After hydrogen reduction treatment, the Ni and Fe in Ni_xFe_y catalysts present in the metallic state (**Figure 2**a,c). Interestingly, the spectra for the Ni_1Fe_1, Ni_2Fe_1, Ni_3Fe_1, and Ni_4Fe_1 catalysts differed from those of the Ni_3Fe_0 and Ni_0Fe_3 samples in the pre-edge region and varied with the Ni:Fe ratio, which is explained by alloying in the Ni_xFe_y samples.[11] However, the XANES spectra of the Ni_1Fe_1, Ni_2Fe_1, Ni_3Fe_1, and Ni_4Fe_1 samples were very similar to Ni_3Fe_0 and Ni_0Fe_3 samples in the rising-edge region, consistent with the presence of metallic Ni and Fe. The EXAFS data (Figure 2b,d) for the LDH precursors and the $NiFe_2O_4$ control sample showed Fe—O bonds and Ni—O scattering paths, typical for iron and nickel oxides, respectively. The Fe–O bonds and Ni–O features were absent in the Ni_xFe_y catalysts, while new Fe-metal and Ni-metal features appeared consistent with the presence of metallic states. In the cases of the Ni_3Fe_1 sample, signals were observed in region 4–5 Å (attributed to the Ni–Fe (Ni) and Fe–Ni (Fe) bonds), which were shifted in position compared to the corresponding features for the Ni_3Fe_0 and Ni_0Fe_3 samples. The shift was increased with the proportion of Ni in the Ni_xFe_y samples, suggesting the gradual formation of Ni_3Fe_1 nanoalloys.

The absorption spectra of all the samples were examined by ultraviolet–visible–near infrared (UV–vis–NIR) diffuse reflectance spectroscopy. As shown in **Figure 3**a and Figure S8, Supporting Information, the LDH precursors displayed strong absorption in the UV region, with some weak absorption in the visible region. In contrast, all Ni_xFe_y catalysts showed strong absorption across the UV, visible and near-infrared regions. Figure 3b temperature measurements show that the Ni_3Fe_1 catalyst had a very strong photothermal effect under a xenon lamp irradiation (PLS-SXE-300DUV, Beijing PerfectLight), with the surface temperature exceeding 300 °C after only 10 min of irradiation. The temperature reached a maximum of around 350 °C after 60 min of irradiation. Under the same irradiation conditions, the surface temperature of the LDH precursor and CaO substrate only reached 220 and 100 °C, respectively. The stronger absorption of the Ni_3Fe_1 catalyst in the visible and NIR regions explained its superior photothermal effect.

Next, the performance of the Ni_xFe_y catalysts and reference catalysts for photo-driven DRM were evaluated in a flow system (0.18 MPa, 75 mL min^{-1}, $CH_4/CO_2/Ar = 25/25/50$). As shown in Figure 3c, the LDH derived Ni_xFe_y catalysts showed excellent photo-driven DRM activity, with the Ni_3Fe_1 catalyst delivering the highest syngas production rate (up to 0.96 mol g^{-1} h^{-1}, with a CO/H_2 ratio of 1.9). CO temperature-programmed desorption (TPD) revealed that Ni_3Fe_1 desorbs CO at lower temperatures than all the other Ni_xFe_y catalysts studied in this work (Figure S9, Supporting Information), thus contributing to its superior syngas production rate. Based on the structural and composition data, surface models of the different catalysts were established (Figures S10–S12, Supporting Information) to calculate the adsorption energies of CH_4 and CO_2 according to the density functional theory (DFT). The results revealed that the adsorption energies of CO_2 on Ni (111) and Fe (111) surfaces were −0.21 and −2.48 eV, respectively, while the adsorption abilities of both surfaces for CH_4 were weak (Ni −0.02 eV, Fe −0.07 eV) (Figures S13 and S14, Supporting Information). For the Ni_3Fe_1 nanoalloys, the adsorption energies for CO_2 and CH_4 on the surface Fe site increased to −3.25 and −2.9 eV, respectively. Therefore, it is hypothesized that the DRM reaction over individual Ni and Fe metals is hindered by the ability to simultaneously adsorb both reactant molecules.

The ultimate goal of photo-driven catalysis is to directly utilize sunlight rather than artificial light sources. A circular quartz convex lens with a diameter of 5 cm was used to concentrate sunlight for sunlight-driven DRM tests. Based on the Ni_3Fe_1 catalyst, a syngas production rate of 0.94 mol g^{-1} h^{-1} was

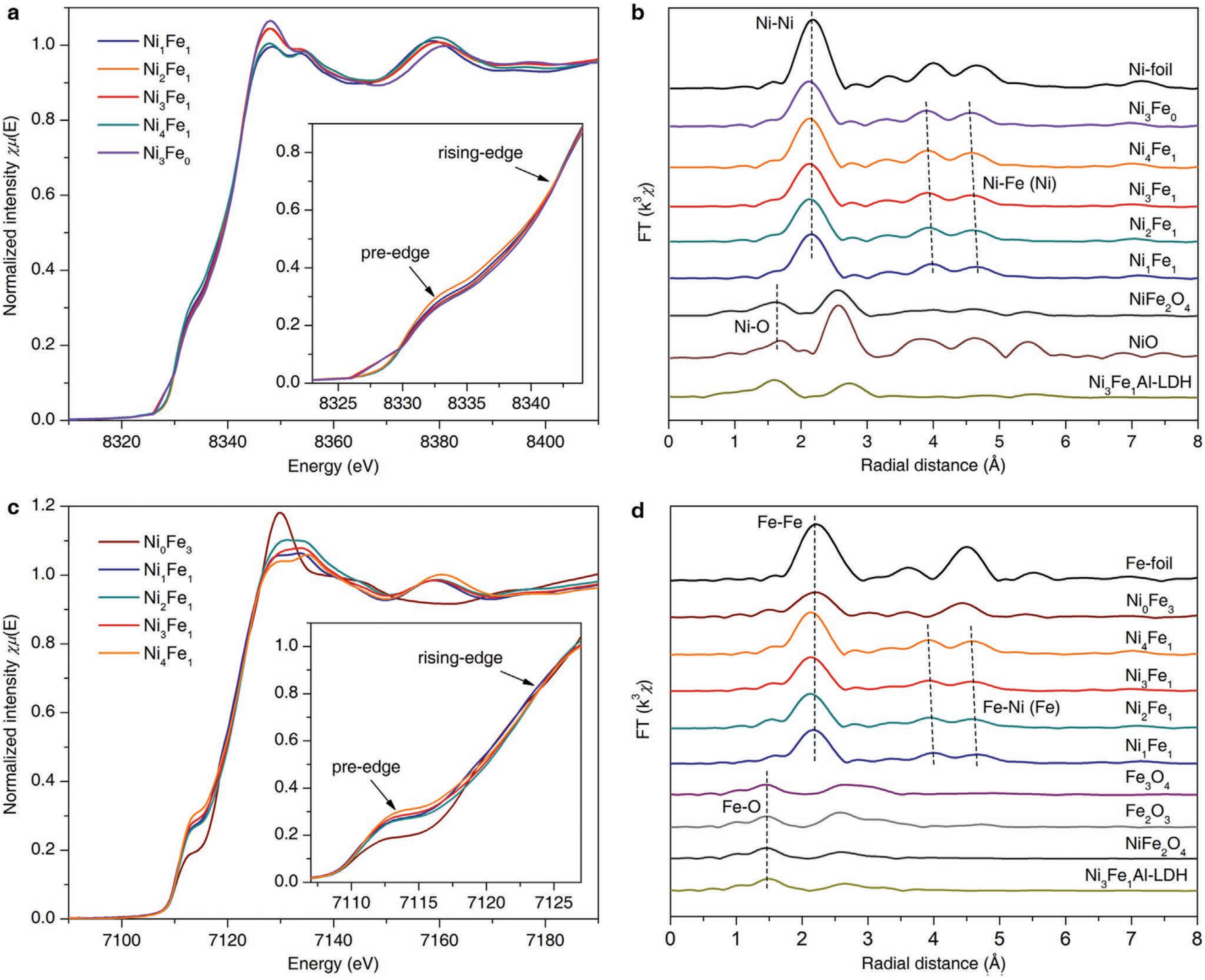

Figure 2. Coordination environment analysis of catalysts. a) Ni K-edge XANES and b) EXAFS spectra of the Ni_xFe_y catalysts, the Ni_3Fe_1Al-LDH precursor, and the $NiFe_2O_4$ control sample. c) Fe K-edge XANES and d) EXAFS spectra of the Ni_xFe_y catalysts, the Ni_3Fe_1Al-LDH precursor, and the $NiFe_2O_4$ control sample.

realized under concentrated sunlight irradiation, very close to the result obtained by xenon lamp irradiation (Figure 3d). The surface temperature of the catalyst under concentrated sunlight reached 330 °C within a few seconds. To our knowledge, this is the first work to report DRM driven by real sunlight. In addition, no significant activity decline was observed for the Ni_3Fe_1 catalyst over 20 h of testing (Figure 3e). The results confirm that photo-driven DRM over the Ni_3Fe_1 catalyst offers a clean and energy-efficient approach for syngas production.

Further DRM tests were carried out at different temperatures and UV/visible light intensities using an electric heating device and light filters (see Experimental Section for details) to explore how incident photons participate in the DRM reaction. **Figure 4**a shows that for electric heating-assisted UV irradiation conditions, the yields of both CO and H_2 over the Ni_3Fe_1 catalyst enhanced along with the increased temperature from 100 to 400 °C. The catalyst showed a syngas yield of 0.84 mol g^{-1} h^{-1} at 350 °C under UV irradiation, which was close to the performance of the full-spectrum photo-driven test. It is worth noting that the syngas production rate reached 46.69 mmol g^{-1} h^{-1} at 100 °C. To our knowledge, this is the lowest temperature for the DRM reaction reported so far. For dark conditions in the temperature range from 300 to 400 °C, the syngas production rate remained at a micromolar level. Syngas production rates of 0.85 and 1.39 mmol g^{-1} h^{-1} were obtained at 350 °C in the dark and under visible irradiation, respectively (Figure S15, Supporting Information), about 1100 and 960 times lower than the photo-driven condition at the same temperature. This indicated the key role of UV light in the photo-driven DRM reaction, with the visible light mainly contributing to a photothermal heating effect. From the Arrhenius plots shown in Figure 4b, the apparent activation energy for DRM over Ni_3Fe_1 was reduced from 57.2 kJ mol^{-1} in the dark to 29.5 kJ mol^{-1} under UV illumination, further demonstrating the special function of UV light beyond the photothermal effect. Figure 4c,d shows the catalytic performance of Ni_3Fe_1 at reaction temperatures of 300

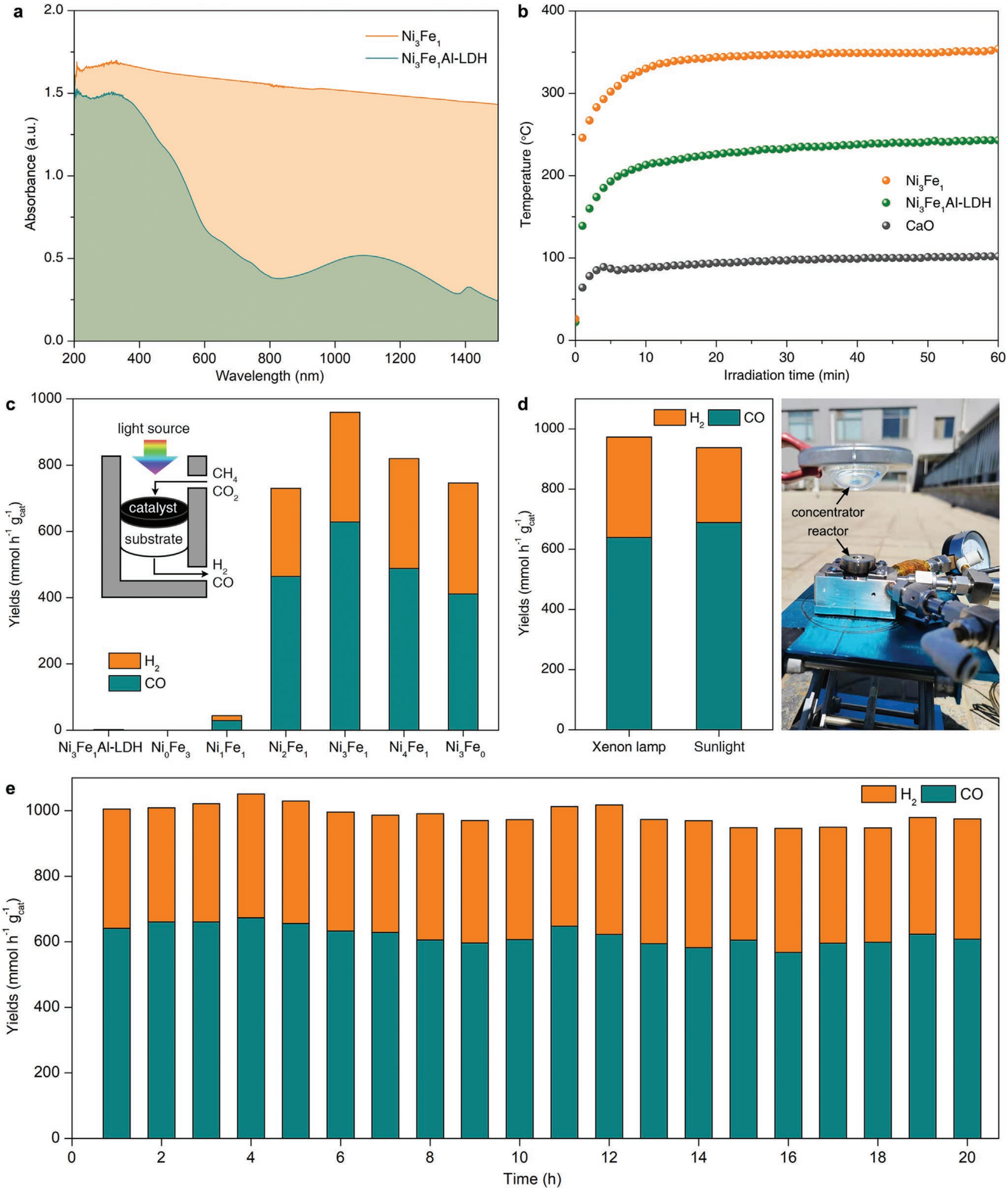

Figure 3. Photo-driven DRM performance. a) UV–vis–NIR absorption spectra for the Ni_3Fe_1 catalyst and Ni_3Fe_1Al-LDH. b) Temperature profiles for the Ni_3Fe_1 catalyst, CaO substrate, and Ni_3Fe_1Al-LDH under UV–vis irradiation. Light intensity = 3.62 W cm^{-2}. c) Reaction device diagram and yields of CO and H_2 for photo-driven DRM reaction of the Ni_3Fe_1Al-LDH precursor and Ni_xFe_y catalysts. d) CO and H_2 yields for the Ni_3Fe_1 catalyst under a xenon lamp and concentrated solar energy at the same temperature (350 °C). A picture of the sunlight concentrating system is shown. e) Stability test for Ni_3Fe_1 under UV–vis irradiation (0.18 MPa, 75 mL min^{-1}, $CH_4/CO_2/Ar = 25/25/50$).

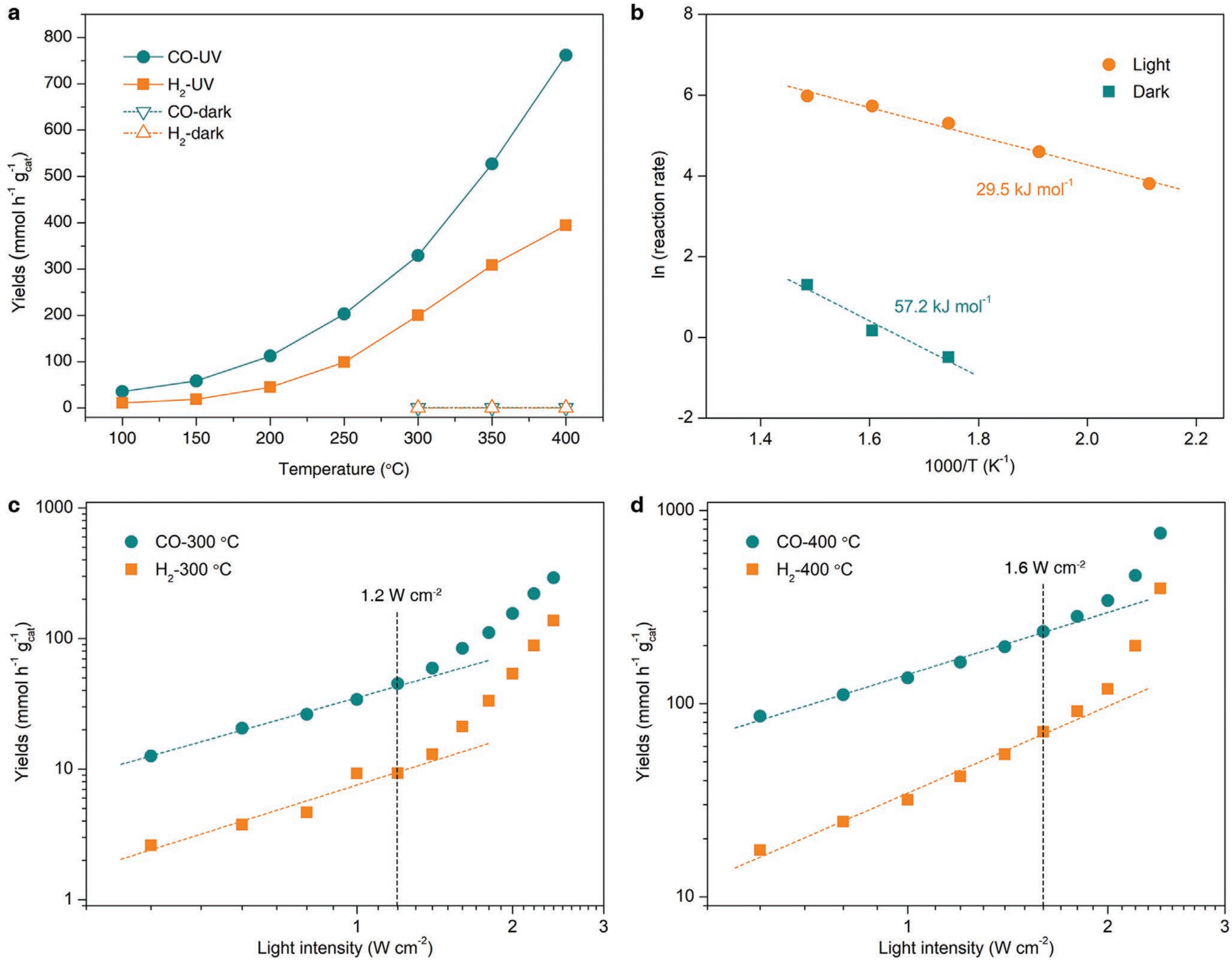

Figure 4. Photothermal synergistic effect study. a) CO and H_2 yields of different temperatures for Ni_3Fe_1 under dark and light conditions. b) Reaction activation energy under light and dark conditions for Ni_3Fe_1. c) Catalytic performance of Ni_3Fe_1 for DRM at 300 °C and different light intensities. d) Catalytic performance of Ni_3Fe_1 for DRM at 400 °C and different light intensities.

and 400 °C as a function of UV intensity. At both temperatures, linear and superlinear growth regions appear upon increasing the UV intensity from 0.2 to 2.4 W cm^{-2}, with the turning point occurring at 1.2 and 1.6 W cm^{-2} for 300 and 400 °C conditions. The superlinear phenomenon at high light intensities is typically attributed to hot electron injection from the LSPR effect of metal nanoparticles into antibonding orbitals of adsorbed reactants, thereby weakening bonds in the adsorbed reactant and promoting the activation process.[12] The lower linear-to-superlinear turning point at 300 °C suggests that the possible LSPR enhancement is preferred at lower temperatures. A further piece of evidence that supports the LSPR effect is the enhanced kinetic isotope effect (KIE) (H_2 rate/D_2 rate) under UV irradiation (Figure S16, Supporting Information).[13]

To gain deeper insights about the LSPR effect of Ni_3Fe_1 in the UV region, finite-difference-time-domain simulations were performed. **Figure 5** shows local electric field distributions about Ni_3Fe_1 nanoalloys under irradiation at 230, 330, 430, and 530 nm. Among these, 330 nm irradiation afforded the strongest enhancement ($E^2/E_o{}^2 = 10.2$), consistent with a strong absorption peak of Ni_3Fe_1 at this wavelength (Figure S8b, Supporting Information). The simulation result suggests that the LSPR effect of Ni_3Fe_1 nanoalloys centered at 330 nm contributes to the improved DRM performance.

To further explore the mechanism of the LSPR effect in promoting the DRM reaction, intermediate species formed during the reaction were investigated by in situ diffuse reflectance infrared Fourier transform (DRIFT) spectroscopy. The DRIFT experiment was divided into three continuous stages: 1) adsorption of reactants at 25 °C, 2) heating in the dark to 300 °C, and 3) heating at 300 °C with light irradiation (**Figure 6**a and Figure S17, Supporting Information). After the addition of the reaction gas at 25 °C, characteristic infrared peaks of CO_2 and CH_4 in the gas phase were observed at 2349 and 3015 cm^{-1}, respectively.[14] With increasing exposure time of the Ni_3Fe_1 catalyst to the CO_2 and CH_4 gas mixture, peaks of adsorbed *CO_2 species appeared

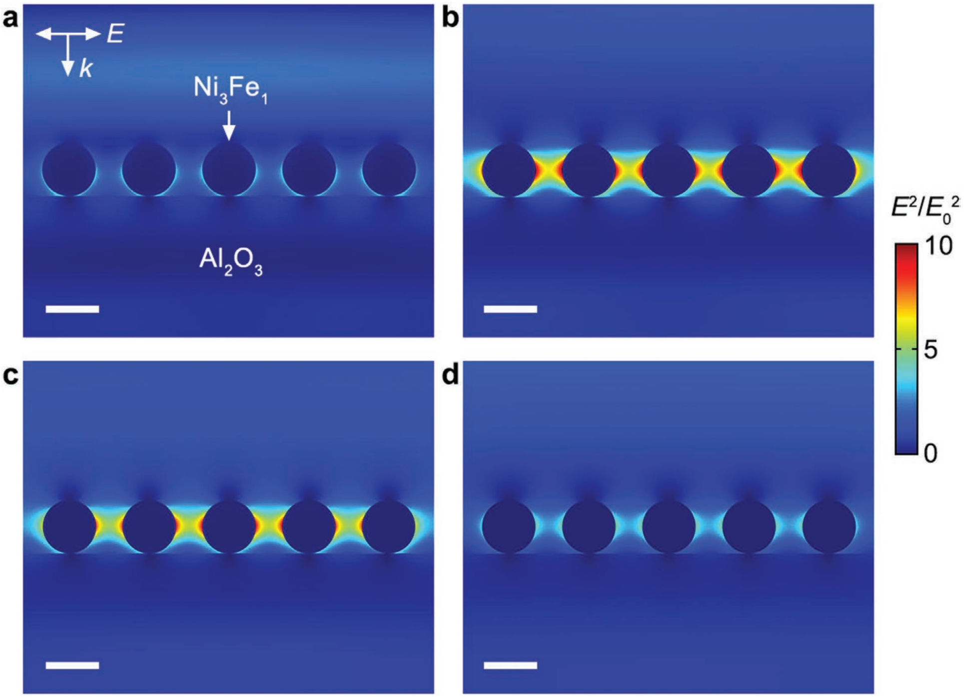

Figure 5. Simulated spatial distribution of the electric field enhancement. Ni_3Fe_1 at a) 230 nm wavelength, b) 330 nm wavelength, c) 430 nm wavelength, and d) 530 nm wavelength. Scale bar: 20 nm. *E* and *k* refer to the direction of electric field and external light source, respectively, and E^2/E_0^2 refers to electromagnetic field intensity.

(centered at 1450 and 1625 cm^{-1}).[14] Next, the reactor was heated to 300 °C, whereupon the peaks due to the adsorbed $*CO_2$ species were attenuated, while a new peak due to more active adsorbed $*CO_2$ species at 1594 cm^{-1} appeared.[15] Results suggested that CO_2 could be activated simply by heating.[14–15] It is worth noting that the characteristic peak of gas-phase CH_4 remained almost unchanged during heating to 300 °C in the dark, with no peaks due to adsorbed $*CH_4$ or derived species being identified. Hence, it is concluded that CH_4 was not activated under dark conditions. When UV was introduced, the peaks associated with adsorbed $*CO_2$ changed obviously, while new peaks appeared at wavenumbers between 2800 and 2900 cm^{-1} due to activated $*CH_4$ species.[16] As the irradiation time increased, a broad peak appeared in the 1700–1900 cm^{-1} region, which was ascribed to a *CHO reaction intermediate.[17] Further, a peak due to the adsorbed *CO product was also observed in 2000–2100 cm^{-1} region.[6b,18] Based on the DRIFT spectra, it can be concluded that at 300 °C in the dark, only CO_2 was activated by the Ni_3Fe_1 catalyst. While UV light contributes to a promoted CH_4 activation process, which is widely recognized as the rate-determining step in low-temperature DRM reactions. Electron paramagnetic resonance (EPR) experiments were then performed (Figure S18, Supporting Information). Under dark conditions, there were no free radicals being detected. When UV light was introduced, an EPR signal with six peaks appeared, typical for methyl radicals. It is worth mentioning that the methyl radical signal appeared even at room temperature, providing strong evidence that CH_4 is activated by Ni_3Fe_1 through a photochemical route rather than a photothermal route. Combining above experiments and simulations, a mechanism for photothermal synergistic DRM effect over the Ni_3Fe_1 nanoalloys was proposed (Figure 6b). Under dark and visible irradiation conditions, only CO_2 could be thermally activated effectively, thus DRM showed a relatively high apparent activation energy. Under UV irradiation, hot electrons generated by the LSPR effect of the Ni_3Fe_1 nanoalloys could inject into the antibonding orbitals of the adsorbed CH_4 molecule, therefore strongly activating methane and significantly lowering the activation energy of the DRM reaction.

3. Conclusion

A novel alumina-supported Ni_3Fe_1 nanoalloy catalyst fabricated by hydrogen reduction of a NiFeAl-LDH precursor showed outstanding performance for the photothermal synergistic DRM reaction. A combination of finite element simulations and in situ infrared spectroscopy established that the remarkable photo-driven DRM performance of the Ni_3Fe_1 nanoalloy catalysts was due to an LSPR effect under ultraviolet irradiation (hot electron injection into antibonding orbitals of CH_4, thus strongly activating methane toward reaction with CO_2) and a photothermal heating effect under visible irradiation. This synergistic effect dramatically lowers the apparent activation energy of DRM, achieving a syngas yield of 0.96 mol g^{-1} h^{-1} with sunlight-driven feasibility and long-term durability and allowing the reaction to proceed at low temperatures (as low as 100 °C). The findings of this study demonstrate a sustainable way to convert methane and carbon dioxide into value-added chemicals.

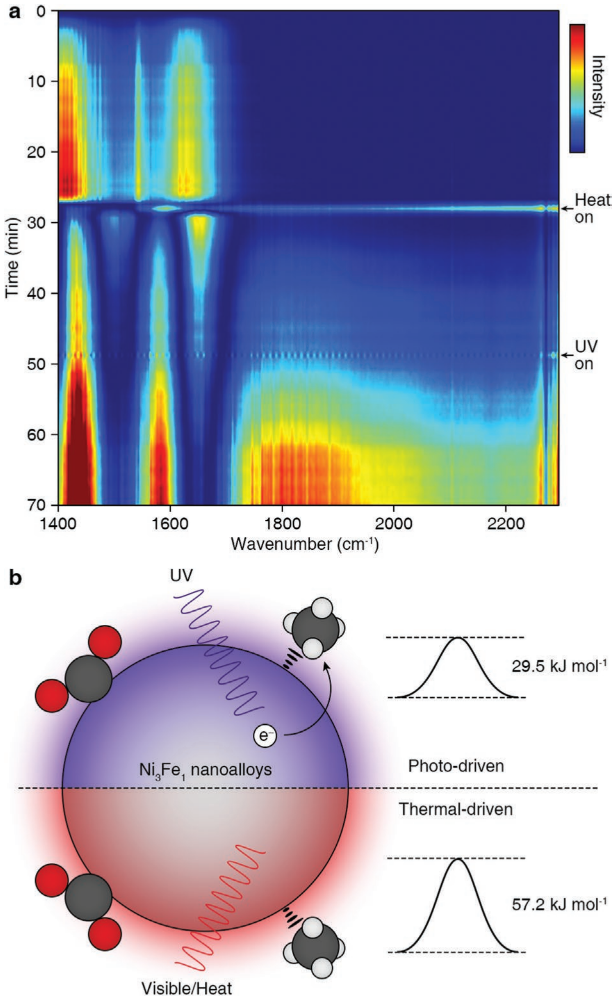

Figure 6. Mechanism of photo-driven DRM. a) In situ DRIFT spectra for photo-driven DRM reaction on Ni_3Fe_1. The spectra were collected at a resolution of 4 cm^{-1} and time intervals of 1 min. The spectrum is divided into upper, middle, and lower parts, corresponding to room temperature in the dark, 300 °C in the dark, and UV light irradiation at 300 °C, respectively. The depth of the color indicates the intensity of the characteristic peak from blue (weak) to red (strong). b) Schematic illustration for the photo-driven DRM reaction over the Ni_3Fe_1 nanoalloys.

Acknowledgements

The authors are grateful for financial support from the National Key Projects for Fundamental Research and Development of China (2018YFB1502002), the National Natural Science Foundation of China (51825205, 52120105002, 21902168, 22088102), the Beijing Natural Science Foundation (2191002), the Strategic Priority Research Program of the Chinese Academy of Sciences (XDB17000000), the CAS Project for Young Scientists in Basic Research (YSBR-004), the Royal Society-Newton Advanced Fellowship (NA170422), and the Youth Innovation Promotion Association of the CAS. The XAFS experiments were conducted in 1W1B beamline of Beijing Synchrotron Radiation Facility (BSRF). G.I.N.W. acknowledges funding support from the Energy Education Trust of New Zealand, the MacDiarmid Institute for Advanced Materials and Nanotechnology, and the Dodd Walls Centre for Photonic and Quantum Technologies.

Conflict of Interest

The authors declare no conflict of interest.

Keywords

CH_4 reforming, CO_2 reduction, layered double hydroxide, photothermal catalysis

---

[1] a) T. P. Hughes, A. H. Baird, D. R. Bellwood, M. Card, S. R. Connolly, C. Folke, R. Grosberg, O. Hoegh-Guldberg, J. B. C. Jackson, J. Kleypas, J. M. Lough, P. Marshall, M. Nyström, S. R. Palumbi, J. M. Pandolfi, B. Rosen, J. Roughgarden, *Science* **2003**, *301*, 929; b) J. A. Patz, D. Campbell-Lendrum, T. Holloway, J. A. Foley, *Nature* **2005**, *438*, 310; c) R. Snoeckx, A. Bogaerts, *Chem. Soc. Rev.* **2017**, *46*, 5805; d) J. Zhang, M. Zhang, S. Chen, X. Wang, Z. Zhou, Y. Wu, T. Zhang, G. Yang, Y. Han, Y. Tan, *Chem. Commun.* **2019**, *55*, 973.

[2] X. Chen, Y. Li, X. Pan, D. Cortie, X. Huang, Z. Yi, *Nat. Commun.* **2016**, *7*, 12273.

[3] a) L. Liu, A. V. Puga, J. Cored, P. Concepción, V. Pérez-Dieste, H. García, A. Corma, *Appl. Catal., B* **2018**, *235*, 186; b) J. Qiao, Y. Liu, F. Hong, J. Zhang, *Chem. Soc. Rev.* **2014**, *43*, 631; c) P. Gao, S. Li, X. Bu, S. Dang, Z. Liu, H. Wang, L. Zhong, M. Qiu, C. Yang, J. Cai, W. Wei, Y. Sun, *Nat. Chem.* **2017**, *9*, 1019.

[4] G. Chen, G. I. N. Waterhouse, R. Shi, J. Zhao, Z. Li, L.-Z. Wu, C.-H. Tung, T. Zhang, *Angew. Chem., Int. Ed.* **2019**, *58*, 17528.

[5] a) K. Song, M. Lu, S. Xu, C. Chen, Y. Zhan, D. Li, C. Au, L. Jiang, K. Tomishige, *Appl. Catal., B* **2018**, *239*, 324; b) F. Jiao, J. Li, X. Pan, J. Xiao, H. Li, H. Ma, M. Wei, Y. Pan, Z. Zhou, M. Li, S. Miao, J. Li, Y. Zhu, D. Xiao, T. He, J. Yang, F. Qi, Q. Fu, X. Bao, *Science* **2016**, *351*, 1065; c) S. M. Stagg-Williams, F. B. Noronha, G. Fendley, D. E. Resasco, *J. Catal.* **2000**, *194*, 240; d) N. V. R. A. Dharanipragada, L. C. Buelens, H. Poelman, E. De Grave, V. V. Galvita, G. B. Marin, *J. Mater. Chem. A* **2015**, *3*, 16251.

[6] a) D. Pakhare, J. Spivey, *Chem. Soc. Rev.* **2014**, *43*, 7813; b) X. Zhu, P. Huo, Y.-p. Zhang, D.-g. Cheng, C.-j. Liu, *Appl. Catal., B* **2008**, *81*, 132; c) R. N. Bhat, W. M. H. Sachtler, *Appl. Catal., A* **1997**, *150*, 279; d) V. R. Choudhary, B. S. Uphade, A. S. Mamman, *Appl. Catal., A* **1998**, *168*, 33.

[7] a) J. A. Rodriguez, D. C. Grinter, Z. Liu, R. M. Palomino, S. D. Senanayake, *Chem. Soc. Rev.* **2017**, *46*, 1824; b) F. Solymosi, G. Kutsán, A. Erdöhelyi, *Catal. Lett.* **1991**, *11*, 149.

[8] a) H. Song, X. Meng, T. D. Dao, W. Zhou, H. Liu, L. Shi, H. Zhang, T. Nagao, T. Kako, J. Ye, *ACS Appl. Mater. Interfaces* **2018**, *10*, 408; b) B. Han, W. Wei, L. Chang, P. Cheng, Y. H. Hu, *ACS Catal.* **2016**, *6*, 494; c) H. Liu, X. Meng, T. D. Dao, H. Zhang, P. Li, K. Chang,

T. Wang, M. Li, T. Nagao, J. Ye, *Angew. Chem., Int. Ed.* **2015**, *54*, 11545; d) S. Shoji, X. Peng, A. Yamaguchi, R. Watanabe, C. Fukuhara, Y. Cho, T. Yamamoto, S. Matsumura, M.-W. Yu, S. Ishii, T. Fujita, H. Abe, M. Miyauchi, *Nat. Catal.* **2020**, *3*, 148.

[9] Z. Li, J. Liu, Y. Zhao, G. I. N. Waterhouse, G. Chen, R. Shi, X. Zhang, X. Liu, Y. Wei, X.-D. Wen, L.-Z. Wu, C.-H. Tung, T. Zhang, *Adv. Mater.* **2018**, *30*, 1800527.

[10] Y. Zhao, Z. Li, M. Li, J. Liu, X. Liu, G. I. N. Waterhouse, Y. Wang, J. Zhao, W. Gao, Z. Zhang, R. Long, Q. Zhang, L. Gu, X. Liu, X. Wen, D. Ma, L.-Z. Wu, C.-H. Tung, T. Zhang, *Adv. Mater.* **2018**, *30*, 1803127.

[11] N. J. Divins, D. Kordus, J. Timoshenko, I. Sinev, I. Zegkinoglou, A. Bergmann, S. W. Chee, S. Widrinna, O. Karslıoğlu, H. Mistry, M. Lopez Luna, J. Q. Zhong, A. S. Hoffman, A. Boubnov, J. A. Boscoboinik, M. Heggen, R. E. Dunin-Borkowski, S. R. Bare, B. R. Cuenya, *Nat. Commun.* **2021**, *12*, 1435.

[12] a) S. Linic, P. Christopher, D. B. Ingram, *Nat. Mater.* **2011**, *10*, 911; b) X. Zhang, X. Li, D. Zhang, N. Q. Su, W. Yang, H. O. Everitt, J. Liu, *Nat. Commun.* **2017**, *8*, 14542.

[13] a) H. Song, X. Meng, Z.-j. Wang, Z. Wang, H. Chen, Y. Weng, F. Ichihara, M. Oshikiri, T. Kako, J. Ye, *ACS Catal.* **2018**, *8*, 7556; b) Z.-j. Wang, H. Song, H. Pang, Y. Ning, T. D. Dao, Z. Wang, H. Chen, Y. Weng, Q. Fu, T. Nagao, Y. Fang, J. Ye, *Appl. Catal. B* **2019**, *250*, 10.

[14] F. Wang, S. He, H. Chen, B. Wang, L. Zheng, M. Wei, D. G. Evans, X. Duan, *J. Am. Chem. Soc.* **2016**, *138*, 6298.

[15] J. Mascetti, M. Tranquille, *J. Phys. Chem.* **1988**, *92*, 2177.

[16] a) L. Wang, L. Wang, J. Zhang, X. Liu, H. Wang, W. Zhang, Q. Yang, J. Ma, X. Dong, S. J. Yoo, J.-G. Kim, X. Meng, F.-S. Xiao, *Angew. Chem., Int. Ed.* **2018**, *57*, 6104; b) N. Nomura, T. Tagawa, S. Goto, *Appl. Catal., A* **1998**, *166*, 321.

[17] a) T. H. Tan, B. Xie, Y. H. Ng, S. F. B. Abdullah, H. Y. M. Tang, N. Bedford, R. A. Taylor, K.-F. Aguey-Zinsou, R. Amal, J. Scott, *Nat. Catal.* **2020**, *3*, 1034; b) R. Yang, Y. Fu, Y. Zhang, N. Tsubaki, *J. Catal.* **2004**, *228*, 23.

[18] L. F. Liao, C. F. Lien, D. L. Shieh, M. T. Chen, J. L. Lin, *J. Phys. Chem. B* **2002**, *106*, 11240.